

## A tunable fiber-coupled optical cavity for agile enhancement of detector absorption

Robert M. Heath, Michael G. Tanner, Robert A. Kirkwood, Shigehito Miki, Richard J. Warburton, and Robert H. Hadfield

Citation: [Journal of Applied Physics](#) **120**, 113101 (2016); doi: 10.1063/1.4962456

View online: <http://dx.doi.org/10.1063/1.4962456>

View Table of Contents: <http://scitation.aip.org/content/aip/journal/jap/120/11?ver=pdfcov>

Published by the [AIP Publishing](#)

---

### Articles you may be interested in

[Inhomogeneous critical current in nanowire superconducting single-photon detectors](#)

[Appl. Phys. Lett.](#) **105**, 222602 (2014); 10.1063/1.4903071

[Superconducting nanowire single photon detectors fabricated from an amorphous Mo<sub>0.75</sub>Ge<sub>0.25</sub> thin film](#)

[Appl. Phys. Lett.](#) **105**, 022602 (2014); 10.1063/1.4890277

[Superconducting nanowire single photon detector on diamond](#)

[Appl. Phys. Lett.](#) **104**, 122602 (2014); 10.1063/1.4869574

[Nanowire-based refractive index sensor on the tip of an optical fiber](#)

[Appl. Phys. Lett.](#) **102**, 213114 (2013); 10.1063/1.4808088





[Superconducting nanowire single-photon detector in an optical cavity for front-side illumination](#)

[Appl. Phys. Lett.](#) **95**, 191110 (2009); 10.1063/1.3263715

---



## Instruments for Advanced Science

 <p><b>Gas Analysis</b></p> <ul style="list-style-type: none"><li>dynamic measurement of reaction gas streams</li><li>catalysis and thermal analysis</li><li>molecular beam studies</li><li>dissolved species probes</li><li>fermentation, environmental and ecological studies</li></ul>	 <p><b>Surface Science</b></p> <ul style="list-style-type: none"><li>UHV TPD</li><li>SIMS</li><li>end point detection in ion beam etch</li><li>elemental imaging - surface mapping</li></ul>	 <p><b>Plasma Diagnostics</b></p> <ul style="list-style-type: none"><li>plasma source characterization</li><li>etch and deposition process reaction</li><li>kinetic studies</li><li>analysis of neutral and radical species</li></ul>	 <p><b>Vacuum Analysis</b></p> <ul style="list-style-type: none"><li>partial pressure measurement and control of process gases</li><li>reactive sputter process control</li><li>vacuum diagnostics</li><li>vacuum coating process monitoring</li></ul>
--	---	---	---

Contact Hiden Analytical for further details:  
**W** [www.HidenAnalytical.com](http://www.HidenAnalytical.com)  
**E** [info@hiden.co.uk](mailto:info@hiden.co.uk)  
**CLICK TO VIEW** our product catalogue

# A tunable fiber-coupled optical cavity for agile enhancement of detector absorption

Robert M. Heath,<sup>1,a),b)</sup> Michael G. Tanner,<sup>1,2,b)</sup> Robert A. Kirkwood,<sup>1</sup> Shigehito Miki,<sup>3</sup> Richard J. Warburton,<sup>4</sup> and Robert H. Hadfield<sup>1</sup>

<sup>1</sup>*School of Engineering, University of Glasgow, Glasgow G12 8QQ, Scotland*

<sup>2</sup>*School of Engineering and Physical Sciences, Heriot-Watt University, Edinburgh EH14 4AS, Scotland*

<sup>3</sup>*Advanced ICT Research Institute, National Institute of Information and Communications Technology, 588-2, Iwaoka, Iwaoka-cho, Nishi-ku, Kobe, Hyogo 651-2492, Japan*

<sup>4</sup>*Department of Physics, University of Basel, Basel, Switzerland*

(Received 17 June 2016; accepted 28 August 2016; published online 15 September 2016)

Maximizing photon absorption into thin active structures can be the limiting factor for photodetector efficiency. In this work, a fiber-coupled tunable cavity is demonstrated, designed to achieve close to unity absorption of photons into a thin film superconducting nanowire single photon detector (SNSPD). A technique for defining a stable cavity between the end of a telecommunications optical fiber and a reflective substrate is described and realized. Cavity resonances are demonstrated both through the tuning of input wavelength and cavity length. The resulting optical cavity can tune the resonant absorption *in situ* over a wavelength range of 100 nm. This technique is used to maximize the single photon absorption into both a back-side-coupled Au mirror SNSPD and a front-side-coupled distributed Bragg reflector cavity SNSPD. The system detection efficiency (SDE) is limited by imperfections in the thin films, but in both cases we demonstrate an improvement of the SDE by 40% over bare fiber illumination. © 2016 Author(s). All article content, except where otherwise noted, is licensed under a Creative Commons Attribution (CC BY) license (<http://creativecommons.org/licenses/by/4.0/>). [<http://dx.doi.org/10.1063/1.4962456>]

## I. INTRODUCTION

A limiting factor for superconducting nanowire single photon detector (SNSPDs)<sup>1</sup> to achieve unity system detection efficiency (SDE) has been achieving high absorption of incident light into the nanowire.<sup>2</sup> In previous work demonstrating the principles of an optical-cavity embedded SNSPD, a radiation absorptance for NbN of only 10%–21% depending on incident polarization at a wavelength of 1550 nm was calculated.<sup>3</sup> Improving this is thus key to achieving an efficient detection technology. One of the simplest routes to improve absorption is to reflect the unabsorbed light back through the detector by positioning a reflector behind the SNSPD. This can be thought of as allowing the photon a second pass of the absorber.<sup>4</sup> By replacing the simple reflector with a distributed Bragg reflector (DBR), further enhancement for a given wavelength can be obtained,<sup>5</sup> with simulations showing above 83% absorption.<sup>6</sup>

A more complex way of increasing absorption, injecting light between two reflective surfaces (an optical cavity) has now been widely adopted.<sup>4,7–9</sup> These use two reflective interfaces to create a standing wave with an anti-node situated within the nanowire. Such structures enhance the absorption at the cavity resonance at the expense of decreasing the absorption away from the cavity resonance and ultimately become almost monochromatic devices. State-of-the-art detector designs with an optical cavity typically use metallic

mirrors<sup>8</sup> to enhance performance at a target wavelength with a fixed cavity length.

We present here cavity-enhanced absorption in a superconducting nanowire single photon detector (SNSPDs) by forming a cavity with a fiber with a concave distributed Bragg reflector (DBR) structure attached to the end facet.<sup>10</sup> This results in a cavity mode confined in all three dimensions allowing high  $Q$ -factors to be achieved. Good design ensures high input coupling efficiencies into the cavity mode from the propagating mode in the fiber. Significantly, by controlling the vertical position of the fiber end with respect to the superconducting nanowire single photon detector (SNSPDs), the cavity mode can be tuned in wavelength facilitating control over the wavelength at which the absorption is maximized. We present here proof-of-principle experiments on this fiber-cavity detector. Specifically, we test two detector configurations: configuration I, a back-side-coupled device with a simple gold reflector, and configuration II, a front-side-coupled detector patterned on a DBR substrate. Tuning of the cavity is performed using a combination of continuous wave (CW) lasers to tune wavelength and low-temperature piezoelectric positioners to tune cavity length. The cavity has stable modes at optical cavity lengths  $<250\ \mu\text{m}$ . Simulations suggest absorption into the device using this technique can reach  $>90\%$ , which could allow, for instance, long-distance demonstrations of loophole-free Bell tests.<sup>11</sup>

The proof-of-concept cavity-enhanced absorption system presented here is original in that its cavity length may be tuned as required. Furthermore, this work represents the

<sup>a)</sup> Author to whom correspondence should be addressed. Electronic mail: robert.heath@glasgow.ac.uk

<sup>b)</sup> R. M. Heath and M. G. Tanner contributed equally to this work.



first cavity-embedded SNSPD in which both reflectors are DBRs. While the fabrication and implementation of this design is complex, the system could be employed for potential two-dimensional detector materials where sample size is typically only a few microns, and where tightly localized optical absorption would be required for efficient operation, and hard to achieve otherwise.

## II. CAVITY FIBER FABRICATION

Two  $\text{TiO}_2/\text{SiO}_2$  pairs were commercially evaporated onto a glass microlens array, atop a half-wavelength  $\text{TiO}_2$  layer to allow easier separation from the array. The reflectivity was chosen to maximize the power inside the cavity: the DBR should be reflective enough to keep light in the cavity, but equally weak enough that light is still able to enter from the fiber. For the designed system, simulation showed that the individual component had a reflectivity of  $\approx 35\%$  at a wavelength of 1550 nm. An optical fiber ferrule was brought into alignment with a microlens by using an infrared camera and microscope to position a 1550 nm optical spot from the fiber in the center of an individual microlens (radius  $r = 250 \mu\text{m}$ ). An adhesive was added to the fiber ferrule, and the components were brought into contact and allowed to cure. Once cured, the components were separated, lifting the DBR layers off the microlens array and leaving them attached to the fiber ferrule, while maintaining the profile of the microlens. This is shown in Figure 1. A release layer

between the DBR and glass microlens is essential in this process, and choice of adhesive is critical for achieving both good lift-off and optical properties, as a thin layer will be included in the final optical stack.<sup>12</sup>

Integration of the DBR into a standard optical fiber ferrule allows the whole system to be connected via optical fiber in our standard cryostat.<sup>13–16</sup> The ferrule is mounted on top of a stack of nano-positioners (attocube systems AG, Germany) allowing fine-tuning of the cavity length and optical spot position.

Curvature of the microlens is transferred to the DBR layers in the final cavity. The curvature was chosen to give a compromise between a long cavity with stable modes and a small spot size. For  $r = 250 \mu\text{m}$  curvature, a cavity with stable modes is expected up to an optical cavity length of  $250 \mu\text{m}$ , with a spot size (beam waist) at the device of sub- $10 \mu\text{m}$  in the ideal case. Alignment of fiber core to the centre of the DBR was challenging as the adhesive had to be cured at  $23^\circ\text{C}$  for 48 h, over which time thermal expansion of the alignment system could easily move the fiber position relative to the lens. From visual inspection, the final alignment is offset by about  $15 \mu\text{m}$  from the center of the microlens feature, shown in Figure 1(f), so some input light may escape the cavity mode. However, profiling cavity behavior (Figure 4) shows the cavity operating in line with design simulation, and there is good agreement between simulated and measured Q-factor and finesse, so we believe that this offset does not significantly alter the behavior of the cavity.

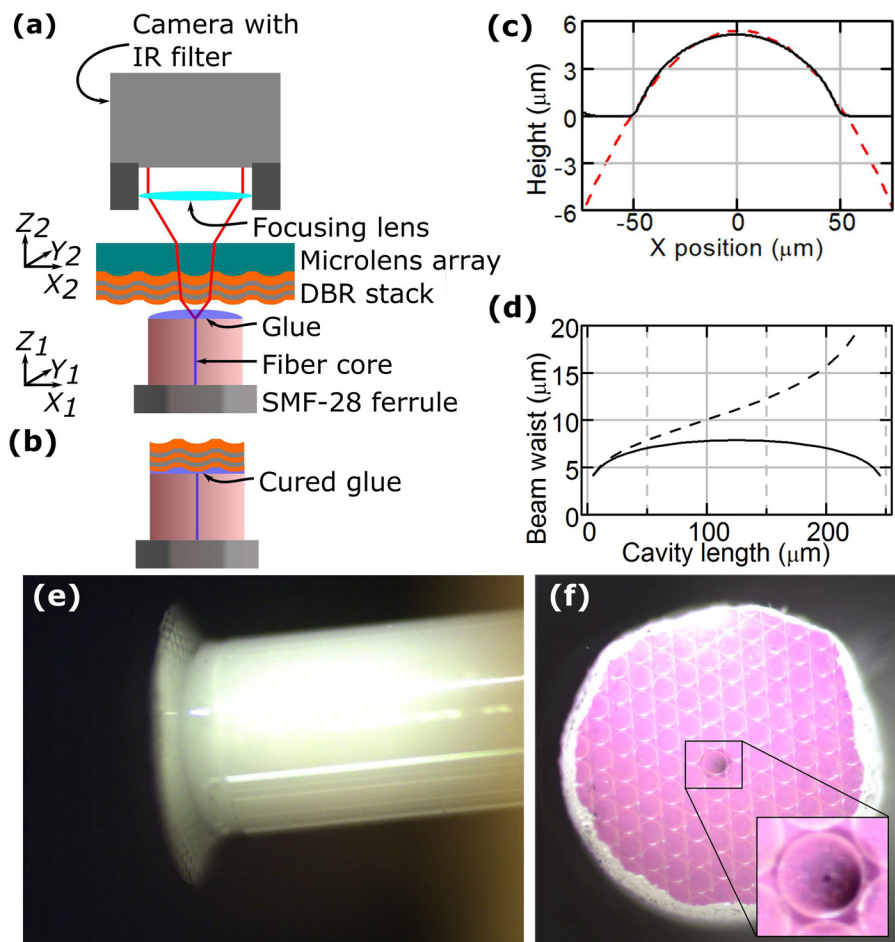


FIG. 1. Fiber DBR alignment. (a) Alignment rig with two independent XYZ stages. The SMF-28 ferrule is aligned with the DBR-coated microlens array. (b) Schematic of the ferrule after lift-off. The DBR layers adhere to the ferrule. (c) Curvature of the microlens, as measured with a Dektak Profilometer. Red dashed line is a circle, radius  $250 \mu\text{m}$ . Microlens profile is described well by a circular profile. Microlens size is approximately  $100 \mu\text{m}$ . (d) Beam waist dimensions for  $r = 250 \mu\text{m}$  curvature DBR, solid line at device, dashed line at concave reflector. Stable cavity modes are expected up to  $250 \mu\text{m}$  optical path length with a sub- $10 \mu\text{m}$  spot size. (e) Profile image of SMF-28 ferrule with attached DBR. (f) End-on image of SMF-28 ferrule with attached DBR. The structure of the microlens array appears as individual circles. Zoom inset: adjusted contrast, the fiber core appears as a small dark spot inside a larger dark area (the fiber cladding), well aligned to the central microlens.

The addition of DBR layers to the end of the optical fiber may naively be assumed to reflect optical signal back up the input fiber, reducing coupling to the detector in the cavity. However, fuller consideration of the complete system shows this is not the case: when the optical cavity including absorbing detector is tuned to resonance the complete system is analogous to an impedance-matched termination in an electrical circuit and, in the ideal case, reflections are reduced to zero. To approach this ideal case, the reflection of the DBR layers on the end of the fiber must be chosen to fit with the reflectance and absorption of the detector structure. If too many DBR layers are deposited on the end of the fiber, a mismatch occurs and light cannot couple efficiently into the cavity. The DBR stack deposited in this experiment consisted of only two repeats of quarter-wavelength dielectric layers. The resulting relatively low-reflectivity DBR matches well with the reflectance of detectors on a variety of cavity substrates. It should be noted that the presence of an absorbing detector on a cavity substrate inherently creates a low-Q factor cavity structure, as Q-factor is dependent on round-trip loss, and achieving high absorption into the film is the aim of this design.

### III. METHODS

Superconducting devices were tested using the low-temperature vibration-damped cryostat developed and employed in other nano-optical studies<sup>13,15</sup> and a system of tunable CW laser sources, attenuators, and polarization controller that operates from 1340 nm to 1650 nm.<sup>16</sup> This allowed the optical cavity to be characterized on tuning, allowing comparison of simulation and experiment. Data

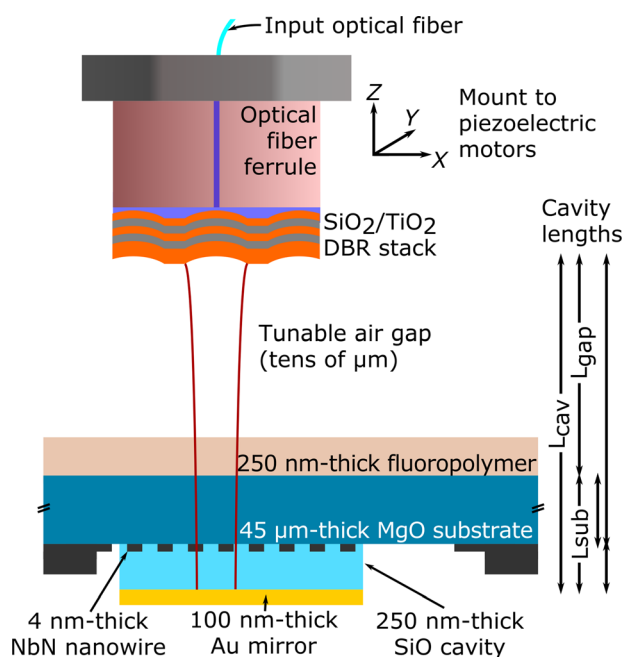


FIG. 2. Schematic of the cavity setup shown for a back side coupled chip. Front side coupling is similar. DBR layers are attached to the end of the optical fiber through a lift-off process. Indication of the form of the cavity mode for a half curved cavity (one curved mirror, one flat) is shown by the red lines in the middle. Cavity lengths are indicated to the right of the cavity structure.

were also taken on replacing the DBR fiber with a bare-end ferrule, creating a simple reflection instead of a cavity. This allowed comparison of the cavity behavior with the regular approach of simple reflectors.

While the low-temperature nano-positioners move in roughly uniform steps, the resistive readout of the Z motor, used for tuning cavity length, had a margin of error that would make it unsuitable for use when measuring small cavity lengths. To allow greater accuracy in the determination of the cavity length, optical coherence tomography (OCT) was used to measure the cavity length before tuning in Z. Afterwards, the position was measured again. Due to the uniform movement, this allows intermediate cavity lengths to be inferred and achieves good results. To confirm the cavity length, fringe spacing when sweeping the wavelength for a given Z value can be used. Using the notation from Figure 2, and with each length  $L$  having a respective refractive index  $n$ , interference fringes with varying total cavity length  $L_{cav}$  are described by  $2L_{cav}n_{cav} = N\lambda$  where  $N$  represents an integer number of waves of wavelength  $\lambda$ . Varying wavelength between  $\lambda_1$  and  $\lambda_2$  such that  $\lambda_1 < \lambda_2$  for constant  $L_{cav}$  will produce adjacent fringes when  $\lambda_1 = 2L_{cav}n_{cav}/N$  and  $\lambda_2 = 2L_{cav}n_{cav}/(N-1)$ . This change in wavelength is  $\Delta\lambda = \lambda_2 - \lambda_1$ . Substituting and expanding,  $\Delta\lambda = 2L_{cav}n_{cav}/N(N-1)$ . If  $N$  is very large,  $N \approx N-1$ , so  $\Delta\lambda \approx \lambda_1^2/2L_{cav}n_{cav}$ . As clear in Figure 2,  $L_{cav}n_{cav} = L_{gap}n_{gap} + L_{sub}n_{sub}$ ; substituting and rearranging the equation for  $L_{gap}$ , and simplifying as  $n_{gap} = 1$  because it is a vacuum, we obtain the final equation

$$L_{gap} \approx \frac{\lambda_1^2}{2\Delta\lambda} - L_{sub}n_{sub}. \quad (1)$$

This relies on knowledge of the substrate thickness  $L_{sub}$ , which can be experimentally determined by white light OCT as required.

This work tested two configurations of detector with the DBR tip. Configuration I is shown in Figure 3(a) and is a back-side coupled 4 nm-thick film of NbN with a simple reflector<sup>9</sup> fabricated as 100 nm-wide wires with a 50% fill factor with an active area of  $15 \mu\text{m} \times 15 \mu\text{m}$ . It had a critical current  $I_c$  at 3.4 K of  $8.1 \mu\text{A}$  and 1 kHz dark count rate (DCR) at a bias current  $I_b = 0.94I_c$ .

Configuration II, shown in Figure 3(b), is more complex, and the SNSPD is fabricated on top of a DBR. The DBR was grown by molecular beam epitaxy (MBE) on a GaAs substrate, first by depositing a 200 nm GaAs buffer layer, followed by 30 repeats of alternating 128.4 nm  $\text{Al}_{0.8}\text{Ga}_{0.2}\text{As}$  and 114.9 nm GaAs, the lengths being  $\lambda/4$  for 1550 nm photons in each medium. The final GaAs layer was deposited as  $\lambda/2$  GaAs, to align the node of the standing wave with the SNSPD location, as there is tight spatial localization of the field as a function of wavelength which does not occur when using a simple reflector. Atop the  $\lambda/2$  layer, an 8 nm NbTiN film was deposited and patterned<sup>17</sup> as 90 nm-wide wires with a 50% fill factor with an active area of  $10 \mu\text{m} \times 10 \mu\text{m}$ . It had a critical current  $I_c$  at 3.5 K of  $11.05 \mu\text{A}$  and 1 kHz DCR at a bias current  $I_b = 0.98I_c$ .

When testing the devices with DBR or bare fiber, they were biased such that their dark count rate was 1 kHz. The

critical currents for both devices remained consistent between fiber changes.

In preliminary testing, both configuration I and configuration II detectors showed poor SDE. Both also had low critical currents and evidenced point-like detection when detector response was profiled using the  $X$  and  $Y$  nano-positioners at 3.5 K. Both devices showed strong dependence on bias current  $I_b$  and had no plateau in efficiency, unlike high-quality detectors demonstrated elsewhere.<sup>5</sup> Combining these features, we have strong indications that both devices are constricted.<sup>18</sup> For the configuration I detector, numerous separate measurements were carried out over an extended timespan, and the device was fabricated on an MgO substrate, which is susceptible to degradation in air. The device's performance is significantly worse than devices from the same fabrication batch which have been reported in the literature<sup>9</sup> though that work was conducted at a lower base temperature which would affect device operation.

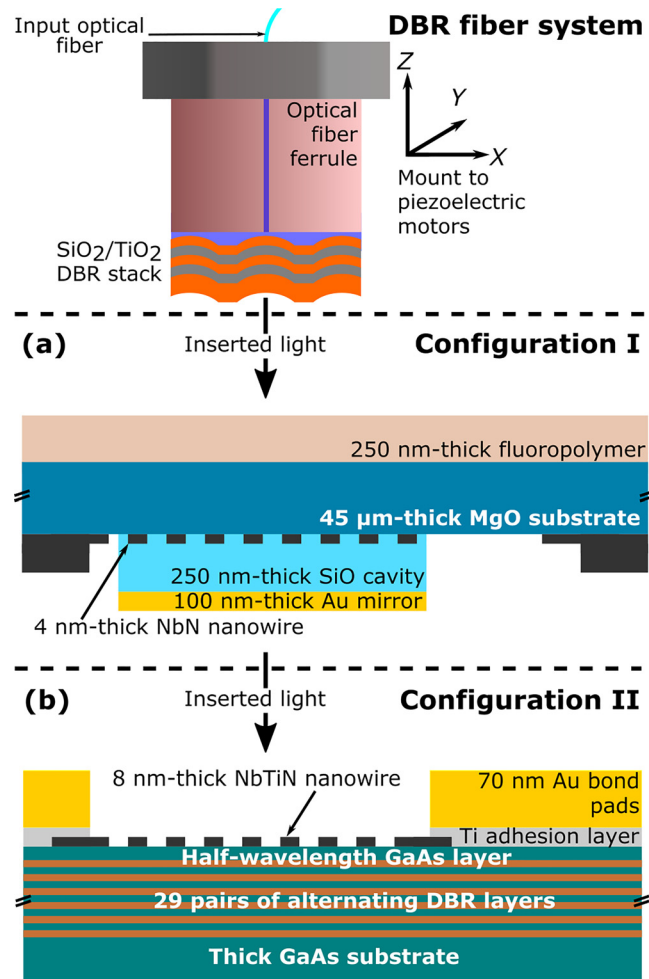


FIG. 3. Diagram of the two optical cavities formed with configurations I and II. In both, light arrives through the fiber ferrule which is mounted on low-temperature piezoelectric nano-positioners, passing through the DBR layers on the tip. This creates a tunable optical cavity with the bottom reflector located behind the SNSPD. In (a), which depicts configuration I, the light is back-side coupled to the SNSPD through 250 nm of anti-reflection fluoropolymer, and a 45 μm thinned MgO substrate. The reflector, 100 nm of gold, is deposited on 250 nm of SiO spacer. In (b), which depicts configuration II, the light is front-side coupled to the SNSPD, and the bottom mirror is a DBR directly beneath the SNSPD.

Meanwhile, the configuration II detector was fabricated in a polycrystalline superconductor (NbTiN) deposited on a DBR. Fabrication in this case was challenging as the DBR had >2 nm peak-to-peak surface roughness leading to an increased likelihood of constrictions.

Using Thin Films Center's Essential Macleod, it is possible to create a one-dimensional model of the behavior of the system as a layered stack. Reducing a three-dimensional system to one dimension requires several assumptions: for the *film*, that the materials used match the index values used in the simulation, and in particular, that the fill-factor of the SNSPD can be approximated as a thinner film; and for the *cavity* that the on-axis behavior can be separated from the lateral confinement by the curved mirror. The system can be approximated as a stack both when using the DBR fiber and when using a bare fiber. However, when the system is modelled with a bare fiber, this fiber should be ignored in the simulation to prevent modelling a physically unlikely plane-parallel cavity. These are very unstable to a small angular misalignment: it is very unlikely one would occur unintentionally in this experiment. Concerning the complex refractive index of the SNSPD, while we have refractive index  $n$  and extinction coefficient  $\kappa$  values for NbN which the SNSPD in configuration I is fabricated from at a range of wavelengths, these are not readily available for NbTiN used in configuration II, and the particular film we have used has not been tested by ellipsometry. Values in the literature

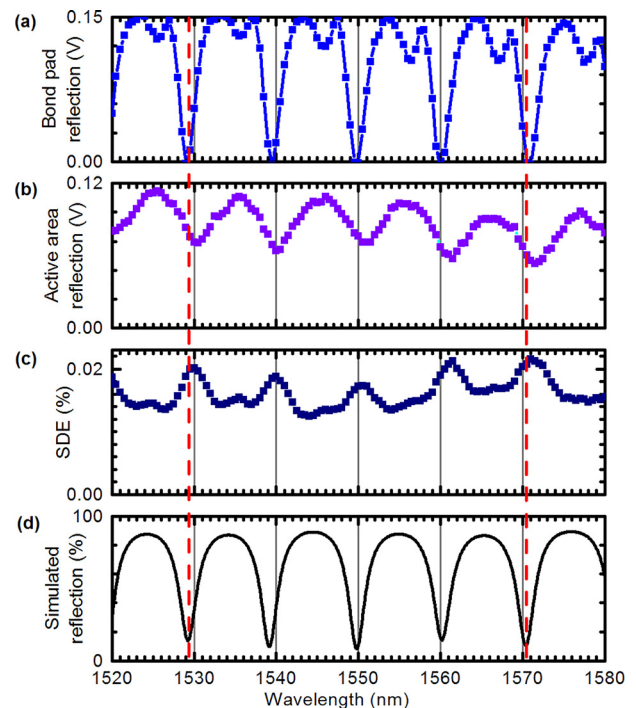


FIG. 4. Cavity behavior in simulation and experiment for the configuration I device when illuminated with a DBR fiber. (a) Experimental reflected power from the bond pads. (b) The reflection when illuminating the SNSPD active area. The Q-factor in (a) is higher than in (b). This is easily explained, as the Q-factor depends on round-trip loss: in (a) the cavity is formed without an absorber, while in (b) there is an absorbing thin film in the cavity. (c) The SDE of the SNSPD at this same point. (a) and (b) are measured in voltage output from an InGaAs single photon avalanche diode (SPAD), after amplification. (d) A one-dimensional simulation of the reflected power from the bond pads, and should be compared to (a).

vary,<sup>4,8,19,20</sup> which is likely a product of the varying relative compositions of the films tested. As such we use established NbN refractive indices in the simulation. For the assumption regarding the fill factor, we note that in previous work it has agreed with experimental data.<sup>4</sup> Finally, as the DBR fiber has a relatively large radius, the focussing of the beam in the cavity is rather gentle such that the cavity mode can be described well with the result of the one-dimensional simulation multiplied by a Gaussian lateral cavity mode.

With these assumptions in mind, we are able to compare the experimental results in Figure 4 with the simulation in Figure 4(d), simulating the configuration I detector by fixing  $L_{gap} = 33.9 \mu\text{m}$  and  $L_{sub} = 45.0 \mu\text{m}$ . As can be seen in the experimental data in Figures 4(a)–4(c), the fringe spacings match well: (a) matches with (d), a like-for-like comparison, while (b) and (c) are shifted slightly to longer wavelengths by the extra length of this cavity. The peaks in the experimental data match nicely with the simulation, and SDE is maximized where reflection is lowest, the principle of the cavity. The red dashed lines across all four figures can be used as a visual guide. Calculating  $L_{gap}$  from the experimental data, we obtain a value of  $34.4 \mu\text{m}$ , in very close agreement with the simulated value. Afterwards, using white-light OCT we observed a strong peak at  $35 \mu\text{m}$ , further confirming these values.<sup>21</sup>

Defining finesse as free spectral range over full-width at half-maximum (FWHM) bandwidth, and Q-factor as finesse multiplied by resonance frequency over free spectral range, in Figure 4(a) the dips in the measured reflection show a finesse of 4.5 and a Q-factor of 660, and the corresponding simulation (d) shows a finesse of 4.4 and Q-factor 650, in close agreement. When measuring reflection from the active device area in (b), the experimental values fall to a finesse of 2.2 and a Q-factor of 320, which can be explained by the presence of the thin film absorber. For configuration II, we determine a finesse of 3.6 and a Q-factor of 185, lower than the values for configuration I, showing that when operating as intended, configuration II creates a cavity with higher losses, which is desirable as this is caused by absorption into the thin film.

Having demonstrated that the simulation of the cavity response matches with experiment, we are able to predict the detector absorption efficiency  $\eta_{absorption}$  as a function of wavelength in the ideal case, Figures 7(c) and 9(c). As shown in Figure 7(c), for configuration I,  $\eta_{absorption}$  can be improved from 60% (bare fiber illumination) to near-unity by the DBR fiber cavity. Figure 9(c) shows the simulated absorption  $\eta_{absorption}$  of configuration II. Due to imprecise fabrication, the resonance of the substrate that was intended to be at 1550 nm was at 1510 nm, shown in the plot of the bare fiber behavior. With the addition of the DBR fiber, it is possible to move this resonance wavelength, and by tuning the cavity length, an  $\eta_{absorption}$  at a wavelength of 1550 nm of  $>70\%$  is possible where it would be  $<30\%$  without.

The coupling efficiency  $\eta_{coupling}$  varies with cavity length, as shown in Figure 5. Over the range bounded by blue lines, when illuminating the detector with a bare fiber, for configuration I  $\eta_{coupling}$  varies from 70% to 75%, and for configuration II  $\eta_{coupling}$  varies from 76% to 86%.

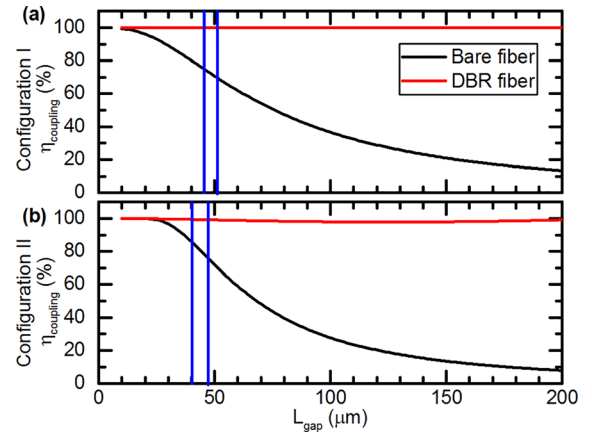


FIG. 5. Calculated coupling efficiencies  $\eta_{coupling}$  shown for configuration I in (a) and configuration II in (b) by fiber type for given air gap length  $L_{gap}$ . Coupling efficiency was calculated as the definite double integral of a 2-dimensional Gaussian with FWHM matching the calculated FWHM beam waist at the detector for gap length  $L_{gap}$ . Limits were chosen to match the respective configuration's active area. The blue lines in (a) and (b) show the limits of  $L_{gap}$  used in Figures 6 and 8, respectively. For configuration I, the distance through the back-side-illuminated substrate and its refractive index are factored into the calculated beam waist.

Illuminating the same systems with the DBR fiber,  $\eta_{coupling}$  remains above 99% in both cases. System detection efficiency is calculated as<sup>22</sup>

$$SDE = \eta_{coupling} \cdot \eta_{absorption} \cdot \eta_{internal} \cdot \eta_{trigger}, \quad (2)$$

where  $\eta_{internal}$  is the probability an absorbed photon generates an observable electrical signal, and  $\eta_{trigger}$  is the efficiency of the counting electronics at registering output. From this, it can be inferred that as the optics in this system should give high  $\eta_{coupling}$  and  $\eta_{absorption}$ , and  $\eta_{trigger}$  is generally near unity, if SDE is low it is probable that this is due to a low  $\eta_{internal}$ . This agrees with the prior evidence of these being constricted devices, as only one region of the detector would be operating near its critical current  $I_c$ , so the internal quantum efficiency would be limited by the reduced relative bias current everywhere except the constricted region.

#### IV. CONFIGURATION I RESULTS

The configuration I SNSPD was cooled to 3.4 K and aligned with the DBR fiber to form a cavity. The wavelength was tuned across a 60 nm range, centered on 1550 nm. The cavity length was also tuned. The result of the experiment and associated simulation is shown in Figure 6. The measured SDE oscillates both as a function of wavelength and cavity length demonstrating a resonant cavity effect. As shown in Figure 7, an improved SDE is obtainable using the tunable cavity over using the bare fiber. The minimum and maximum values are selected from the data shown in Figure 6(a). The bare fiber data were taken in a separate cycle of the closed-cycle cryostat, and while it was matched to the parameters used in (b), it is not perfectly comparable, hence it is plotted separately. Acknowledging this, we can see an increase in the SDE from 0.017% at 1560 nm to, when properly tuned, 0.024%, an improvement of 1.4 times.

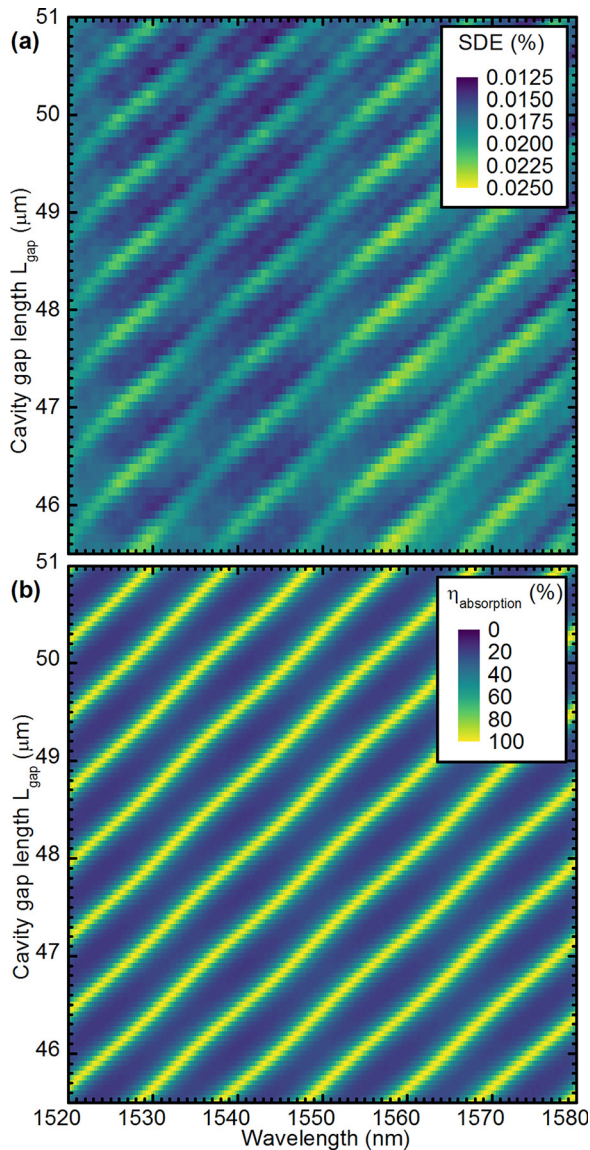


FIG. 6. Tuning behavior of configuration I. (a) The experimental SDE on tuning the cavity, in practice by varying the length from the fiber to the surface of the MgO from  $45.5 \mu\text{m}$  to  $51 \mu\text{m}$ . (b) The simulated absorption  $\eta_{\text{absorption}}$  over the same range. In both cases, the incident photon wavelength is swept from  $1520 \text{ nm}$  to  $1580 \text{ nm}$ . While the variation in the simulated absorption is over a larger range than the variation in SDE, the features are in qualitative agreement.

This simulation in Figure 6 models the 50% fill-factor 4 nm thick nanowire data as a 2 nm thick film. There is a good correspondence with the location of the cavity resonances in the experimental data. However, the contrast is much higher in the simulation: the experimental SDE drops to only a half of the maximum value away from the cavity resonance, yet the simulated absorption drops to a fifth of the maximum value. This perhaps highlights the limitations of the assumptions made to describe the refractive index of the nanowire.

We comment that when using both the bare and DBR fiber, the polarization of the  $1550 \text{ nm}$  input light was adjusted to achieve the maximum count rate. Prior testing of the equipment revealed that the polarization of the laser used varied little over the range, having an effect much smaller

than that of the cavity oscillations over the small range used in this test.

## V. CONFIGURATION II RESULTS

The configuration II SNSPD was cooled to  $3.5 \text{ K}$ . As with the configuration I device, the wavelength was tuned, as was the cavity length, but in this experiment a wider tuning range was used. The experimental results along with a simulation are shown in Figure 8. Again, a clear series of resonances is observed, evidence for cavity effects. As the DBR is distributed over an optical length of about  $23 \mu\text{m}$ , unlike for the simple reflector in configuration I, the length through the substrate material that comprises the DBR  $L_{\text{sub}}$  is less well defined. In order to calculate  $L_{\text{gap}}$ , the fringe spacing of the simulated data was matched to the experimental results.

There is a greater degree of disagreement between the simulation and the experimental result for this device: notably, the experimental fringes appear broader than the simulation. It is possible that this comes from inhomogeneities between theoretically identical layers of the DBR, which could lead to a general “blurring” of the features. Nevertheless, the cavity structure still performs as designed, and the match between experiment and simulation is good at a qualitative level: a strong resonance effect from the cavity is observed. Notably, an increase in the efficiency for photons of  $1550 \text{ nm}$  wavelength can be achieved by *in situ* tuning of the cavity length. The overall tuning range is shown clearly in Figure 9(c).

Unlike in Figure 7, the parameters for positioning the fiber could not be matched for the data in Figure 9, as the dark count rate increased below a certain cavity length, which we attribute to some part of the fiber mount coming into contact with the surface of the SNSPD. Subsequently, we cannot simply calculate a figure of merit comparable to the 1.4 times SDE increase seen for configuration I. However, we can calculate the change in the SDE at the target wavelength ( $1550 \text{ nm}$ ) relative to the peak at ( $1500 \text{ nm}$ ). For the bare fiber shown in Figure 9(b), at  $1550 \text{ nm}$ , the SDE is  $0.49\%$ , compared to a peak value of  $1.47\%$  at  $1500 \text{ nm}$ . So,  $\eta_{1550 \text{ nm}} = 0.33\eta_{1500 \text{ nm}}$ , or the SDE at  $1550 \text{ nm}$  is 33% of that at  $1500 \text{ nm}$ , when there is no DBR fiber. When using a DBR fiber, as shown in Figure 9(a) by tuning correctly it is possible to get an SDE of  $0.17\%$  at  $1550 \text{ nm}$ , and the peak SDE at  $1500 \text{ nm}$  is  $0.37\%$ : so, we have  $\eta_{1550 \text{ nm}, \text{DBR}} = 0.46\eta_{1500 \text{ nm}, \text{DBR}}$ . From this, we can see that the SDE at  $1550 \text{ nm}$  is improved from 0.33 to 0.46 of the maximal SDE at  $1500 \text{ nm}$ , or a response at  $1550 \text{ nm}$  of 46% of that at  $1500 \text{ nm}$ . The improvement in the SDE from 33% to 46% when using the DBR fiber represents an improvement of 1.4 times.

## VI. DISCUSSION

It is clear that the overall benefit of the tunable cavity is to take the effect of the common reflector structure that is widely employed<sup>4-9</sup> and allow a degree of control over the wavelength at which the resonance occurs. From the results presented here for a simple reflector as demonstrated by configuration I, this offers an SDE of 1.4 times the value

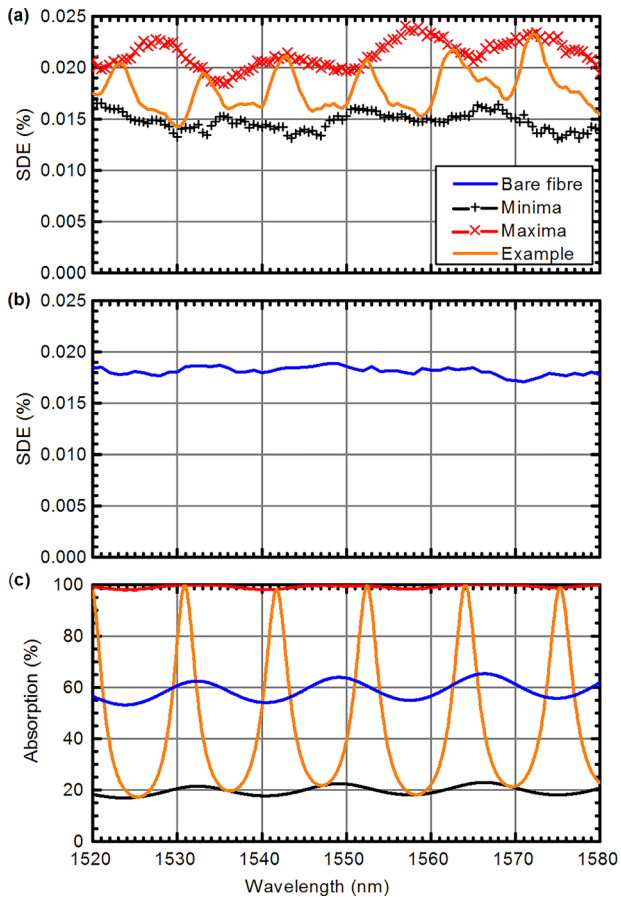


FIG. 7. Graphs of tuning range of configuration I, experiment with DBR fiber shown in (a), experiment with bare fiber shown in (b), and simulation shown in (c). In (c), by varying the cavity length over  $5\ \mu\text{m}$  and making a simulation every  $25\ \text{nm}$ , it was possible to select the absorption maxima and minima. These are shown as red and black lines. The absorption profile for an example single cavity length is shown in orange, and for comparison, the bare fiber result is included in blue. For experimental data, post-selected maxima and minima are shown as individual points. An example set of data is given when using the DBR fiber in (a). The bare fiber data are shown separately, in (b), as the data are not directly comparable, because factors such as the optical spot size might vary between the two experiments. The bare fiber has only a small SDE dependence on wavelength, while the tunable cavity has a more visible oscillation. By forming the cavity with the DBR fiber, an improved count rate is obtained at the wavelengths of the cavity resonances. By tuning the cavity length, one of the resonances can be tuned to  $1550\ \text{nm}$  wavelength.

obtained without a cavity, for incident photons of wavelength  $1560\ \text{nm}$ . Simulation suggests that the absorption should increase by about 1.64 times (from 60% to 99%).

For the configuration II SNSPD fabricated on a DBR reflector, at a wavelength of  $1550\ \text{nm}$  the SDE was also 1.4 times higher. From simulation, an increase of around a factor of two would be expected. Accounting for the same factors as configuration I, and noting the challenges of perfect DBR fabrication that likely lead to a wavelength shift in features between simulation and experiment, the experiment shows a good improvement in the SDE.

There is excellent qualitative agreement between the features seen in the one-dimensional simulation of absorbed power into the nanowire and the experimental results. We do not expect to see identical responses, because the simulations do not consider the other factors that influence the SDE,

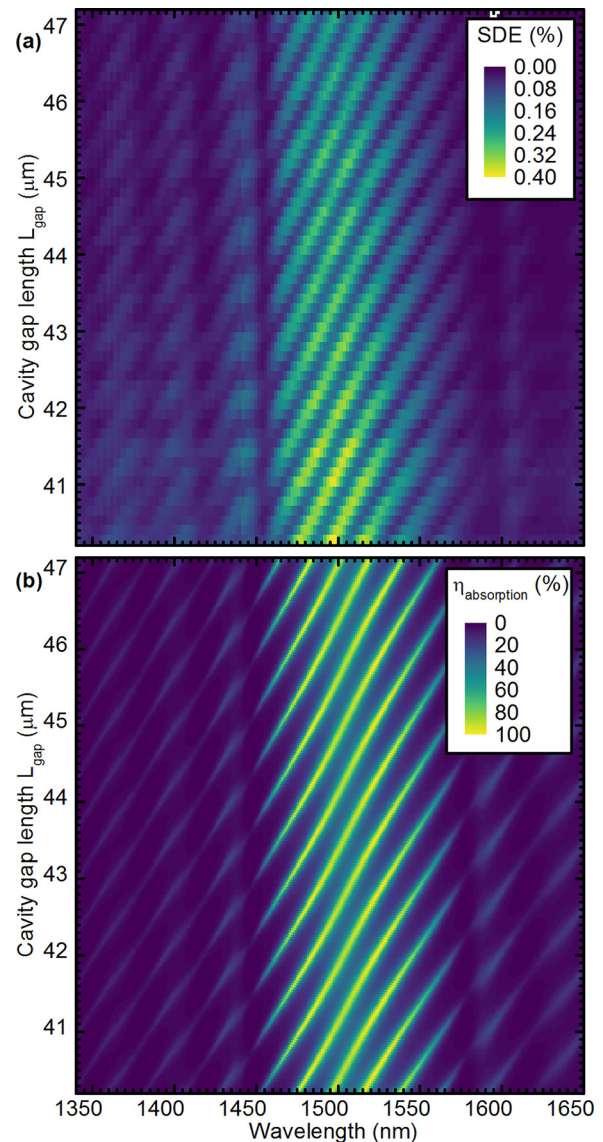


FIG. 8. Tuning configuration II: experimental results and simulation. (a) The experimental SDE on tuning the fiber-to-surface distance by  $40.2\ \mu\text{m}$ – $47.2\ \mu\text{m}$ . (b) A simulation of the absorption in the cavity over the same range. In both cases, the incident photon wavelength is swept from  $1340\ \text{nm}$  to  $1650\ \text{nm}$ . In the experimental data, the SDE reduces as the cavity length is increased, which is not seen in the simulation: this is a limitation of the one-dimensional simulation being unable to model the increase in the spot size and concomitant reduction in  $\eta_{\text{coupling}}$ . The experimental cavity resonances are qualitatively reproduced in the simulation.

such as the polarisation of the input light, and the  $\eta_{\text{coupling}}$  and  $\eta_{\text{internal}}$  coefficients, which will vary. In addition, for the DBR fiber, imperfect centering and adhesive choice will lead to less ideal results than assumed in the simulations here, and for both the DBR fiber and DBR substrate in configuration II, variations in layer thickness during fabrication will lead to disagreement with simulation.

The current state-of-the-art SNSPDs use optical cavities<sup>5,8</sup> to achieve high SDE, constraining the detector to efficient operation at a specific wavelength range, with performance decreasing SDE outside of this. This work presents an agile proof-of-concept system using two DBR reflectors that can be tuned *in situ* over a range of  $100\ \text{nm}$  to optimize as required. This has applications in systems where



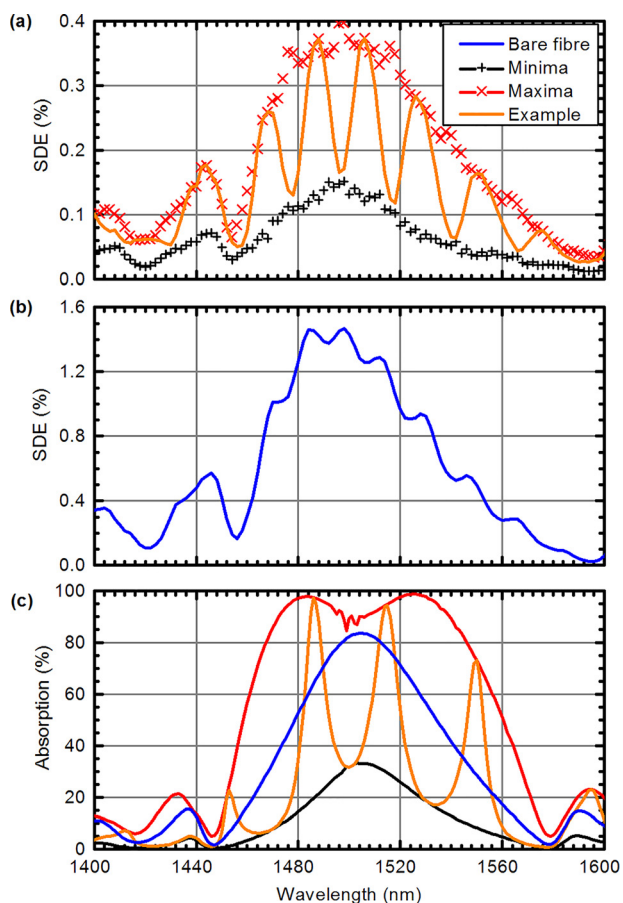


FIG. 9. Wavelength tuning dependence of configuration II, experiment with DBR fiber shown in (a), experimental comparison with bare fiber shown in (b), and simulation shown in (c). In (c), by varying the cavity length over 17  $\mu\text{m}$  and making a simulation every 125 nm, it was possible to select the maxima and minima, shown as red and black lines. The absorption profile for an example single cavity length is shown in orange, and for comparison the bare fiber result is included in blue. As with configuration I data, experimental data are shown in separate graphs as they are not directly comparable. The bare fiber result shows a much higher SDE, but this is because (unlike for the configuration I data) the cavity lengths were unable to be matched. Worthy of note is that off-resonance, at 1550 nm, the tunable cavity offers the opportunity to select a cavity length such that the SDE is maximized at a particular wavelength.

there is a strong dependence on wavelength, where matching peak detector SDE with a precisely defined wavelength is beneficial. Examples include a means to replace narrowband filters in quantum optics experiments with spontaneous parametric down-conversion (SPDC) sources,<sup>23</sup> when detecting fluorescence and luminescence from biological samples,<sup>24</sup> and in characterization of single photon emitters for quantum information networks such as semiconductor quantum dots<sup>25</sup> or nitrogen-vacancy diamond.<sup>26</sup> Using laser ablation to fabricate the DBR fiber<sup>27,28</sup> would allow direct deposition of the DBR layers onto the fiber material, which would both improve alignment, reduce scattering losses and losses associated with index-matching issues caused by the adhesive. A packaged, aligned detector could be imagined with only one piezoelectric motor to allow Z tuning over 1  $\mu\text{m}$ , providing a fully tunable practical package for such experiments. As the DBR tightly localizes the field within a thin spatial zone, the system could also be employed for probing ultrathin layers such as graphene and related two-dimensional materials.

## VII. CONCLUSION

In this work, the SDE of two SNSPDs was measured at a range of wavelengths and cavity spacings, using a bare fiber and using a DBR-coupled fiber. Two configurations of SNSPD were employed, one on a simple reflector and the other on a DBR. The response in both situations matched one-dimensional simulations, and experimentally demonstrated tuning of the cavity resonance, and in turn an enhancement in the SDE at a photon wavelength of 1550 nm. While the proof-of-concept system's SDE is low owing to poor detector performance, the principle that SDE can be dynamically boosted by tuning cavity structure is established and can be applied in the future to state-of-the-art detectors. The tunable nature of the cavity offers some mitigation of the imprecise nature of DBR and cavity fabrication, has applications in experimental work where *in situ* tuning of wavelength is beneficial, and could be simplified for practical use.

## ACKNOWLEDGMENTS

The authors thank the UK Engineering and Physical Sciences Research Council for support. R.H.H. acknowledges a Royal Society University Research Fellowship. R.M.H., M.G.T., R.A.K., and R.H.H. acknowledge EPSRC Grant Code EP/G022151/1 and thank Dr. Ed Clarke at the University of Sheffield, UK for DBR fabrication. R.J.W. acknowledges financial support from NCCR QSIT.

- <sup>1</sup>G. N. Gol'tsman, O. Okunev, G. Chulkova, A. Lipatov, A. Semenov, K. Smirnov, B. Voronov, A. Dzardanov, C. Williams, and R. Sobolewski, *Appl. Phys. Lett.* **79**, 705 (2001).
- <sup>2</sup>C. M. Natarajan, M. G. Tanner, and R. H. Hadfield, *Supercond. Sci. Technol.* **25**, 063001 (2012).
- <sup>3</sup>V. Anant, A. J. Kerman, E. A. Dauler, J. K. W. Yang, K. M. Rosfjord, and K. K. Berggren, *Opt. Express* **16**, 10750 (2008).
- <sup>4</sup>M. G. Tanner, C. M. Natarajan, V. K. Pottapenjarra, J. A. O'Connor, R. J. Warburton, R. H. Hadfield, B. Baek, S. W. Nam, S. N. Dorenbos, E. B. Ureña *et al.*, *Appl. Phys. Lett.* **96**, 221109 (2010).
- <sup>5</sup>F. Marsili, V. B. Verma, J. A. Stern, S. Harrington, A. E. Lita, T. Gerrits, I. Vayshenker, B. Baek, M. D. Shaw, R. P. Mirin, and S. W. Nam, *Nat. Photonics* **7**, 210 (2013).
- <sup>6</sup>A. Gaggero, S. J. Nejad, F. Marsili, F. Mattioli, R. Leoni, D. Bitauld, D. Sahin, G. Hamhuis, R. Nötzel, R. Sanjines, and A. Fiore, *Appl. Phys. Lett.* **97**, 151108 (2010).
- <sup>7</sup>K. M. Rosfjord, J. K. W. Yang, E. A. Dauler, A. J. Kerman, V. Anant, B. M. Voronov, G. N. Gol'tsman, and K. K. Berggren, *Opt. Express* **14**, 527 (2006).
- <sup>8</sup>S. Miki, T. Yamashita, H. Terai, and Z. Wang, *Opt. Express* **21**, 10208 (2013).
- <sup>9</sup>S. Miki, M. Takeda, M. Fujiwara, M. Sasaki, and Z. Wang, *Opt. Express* **17**, 23557 (2009).
- <sup>10</sup>R. J. Barbour, P. A. Dalgarno, A. Curran, K. M. Nowak, H. J. Baker, D. R. Hall, N. G. Stoltz, P. M. Petroff, and R. J. Warburton, *J. Appl. Phys.* **110**, 053107 (2011).
- <sup>11</sup>L. K. Shalm, E. Meyer-Scott, B. G. Christensen, P. Bierhorst, M. A. Wayne, M. J. Stevens, T. Gerrits, S. Glancy, D. R. Hamel, M. S. Allman, K. J. Coakley, S. D. Dyer, C. Hodge, A. E. Lita, V. B. Verma, C. Lambrocco, E. Tortorici, A. L. Migdall, Y. Zhang, D. R. Kumor, W. H. Farr, F. Marsili, M. D. Shaw, J. A. Stern, C. Abellán, W. Amaya, V. Pruneri, T. Jennewein, M. W. Mitchell, P. G. Kwiat, J. C. Bienfang, R. P. Mirin, E. Knill, and S. W. Nam, *Phys. Rev. Lett.* **115**, 250402 (2015).
- <sup>12</sup>T. Steinmetz, Y. Colombe, D. Hunger, T. W. Hänsch, A. Balocchi, R. J. Warburton, and J. Reichel, *Appl. Phys. Lett.* **89**, 111110 (2006).

- <sup>13</sup>M. G. Tanner, L. San Emeterio Alvarez, W. Jiang, R. J. Warburton, Z. H. Barber, and R. H. Hadfield, *Nanotechnology* **23**, 505201 (2012).
- <sup>14</sup>J. A. O'Connor, M. G. Tanner, C. M. Natarajan, G. S. Buller, R. J. Warburton, S. Miki, Z. Wang, S. W. Nam, and R. H. Hadfield, *Appl. Phys. Lett.* **98**, 201116 (2011).
- <sup>15</sup>R. M. Heath, M. G. Tanner, A. Casaburi, M. G. Webster, L. San Emeterio Alvarez, W. Jiang, Z. H. Barber, R. J. Warburton, and R. H. Hadfield, *Appl. Phys. Lett.* **104**, 063503 (2014).
- <sup>16</sup>R. M. Heath, M. G. Tanner, T. D. Drysdale, S. Miki, V. Giannini, S. A. Maier, and R. H. Hadfield, *Nano Lett.* **15**, 819 (2015).
- <sup>17</sup>R. A. Kirkwood, "Superconducting single photon detectors for quantum information processing," Ph.D. thesis, University of Glasgow, to be defended in 2016.
- <sup>18</sup>A. J. Kerman, E. A. Dauler, J. K. W. Yang, K. M. Rosfjord, V. Anant, K. K. Berggren, G. N. Gol'tsman, and B. M. Voronov, *Appl. Phys. Lett.* **90**, 101110 (2007).
- <sup>19</sup>M. K. Akhlaghi, H. Atikian, J. F. Young, M. Loncar, and A. H. Majedi, in Proceedings of the 13th Numerical Simulation of Optoelectronic Devices (NUSOD 2013) (IEEE, 2013).
- <sup>20</sup>S. N. Dorenbos, P. Forn-Diaz, T. Fuse, A. H. Verbruggen, T. Zijlstra, T. M. Klapwijk, and V. Zwiller, *Appl. Phys. Lett.* **98**, 251102 (2011).
- <sup>21</sup>R. M. Heath, "Nano-optical studies of superconducting nanowire devices for single-photon detection," Ph.D. thesis, University of Glasgow, 2015.
- <sup>22</sup>F. Najafi, F. Marsili, V. B. Verma, Q. Zhao, M. D. Shaw, K. K. Berggren, and S. W. Nam, in *Superconducting Devices in Quantum Optics*, edited by R. H. Hadfield and G. Johansson (Springer, 2016), Chap. 1, p. 4.
- <sup>23</sup>C. M. Natarajan, A. Peruzzo, S. Miki, M. Sasaki, Z. Wang, B. Baek, S. Nam, R. H. Hadfield, and J. L. O'Brien, *Appl. Phys. Lett.* **96**, 211101 (2010).
- <sup>24</sup>N. R. Gemmell, A. McCarthy, B. Liu, M. G. Tanner, S. N. Dorenbos, V. Zwiller, M. S. Patterson, G. S. Buller, B. C. Wilson, and R. H. Hadfield, *Opt. Express* **21**, 5005 (2013).
- <sup>25</sup>D. Englund, D. Fattal, E. Waks, G. Solomon, B. Zhang, T. Nakaoka, Y. Arakawa, Y. Yamamoto, and J. Vučković, *Phys. Rev. Lett.* **95**, 013904 (2005).
- <sup>26</sup>T. M. Babinec, B. J. M. Hausmann, M. Khan, Y. Zhang, J. R. Maze, P. R. Hemmer, and M. Lončar, *Nat. Nanotechnol.* **5**, 195 (2010).
- <sup>27</sup>D. Hunger, C. Deutsch, R. J. Barbour, R. J. Warburton, and J. Reichel, *AIP Adv.* **2**, 012119 (2012).
- <sup>28</sup>L. Greuter, S. Starosielec, D. Najer, A. Ludwig, L. Duempelmann, D. Rohner, and R. J. Warburton, *Appl. Phys. Lett.* **105**, 121105 (2014).